The new compact triple system: discovery of bright third star around contact binary using LAMOST-MRS spectra and photometry.

Mikhail Kovalev,[1,2,3]⋆ Azizbek Matekov,[1,4,5] Sufen Guo,[6,1,2,3] Xuefei Chen[1,2,7]
and Zhanwen Han[1,2,7]

[1]*Yunnan Observatories, China Academy of Sciences, Kunming 650216, China*
[2]*Key Laboratory for the Structure and Evolution of Celestial Objects, Chinese Academy of Sciences, Kunming 650011, China*
[3]*International Centre of Supernovae, Yunnan Key Laboratory, Kunming 650216, China*
[4] *University of Chinese Academy of Sciences, Yuquan Road 19, Beijing 100049 Sijingshang Block, China*
[5]*Ulugh Beg Astronomical Institute, Uzbekistan Academy of Sciences, 33 Astronomicheskaya str., Tashkent, 100052, Uzbekistan*
[6]*School of Physical Science and Technology, Xinjiang University, Urumqi, 830046, China*
[7]*Center for Astronomical Mega-Science, Chinese Academy of Sciences, 20A Datun Road, Chaoyang District, Beijing 100012, China*

ABSTRACT

We present a study of the third star orbiting around known contact eclipsing binary J04+25 using spectra from the LAMOST medium-resolution survey (MRS) and publicly available photometry. This is a rare case of a hierarchical triple, where the third star is significantly brighter than the inner contact subsystem. We successfully extracted radial velocities for all three components, using the binary spectral model in two steps. Third star radial velocities have high precision and allow direct fitting of the orbit. The low precision of radial velocity measurements in the contact system is compensated by large number statistics. We employed a template matching technique for light curves to find periodic variation due to the light time travel effect (LTTE) using several photometric datasets. Joint fit of third star radial velocities and LTTE allowed us to get a consistent orbital solution with $P_3 = 941.40 \pm 0.03$ day and $e_3 = 0.059 \pm 0.007$. We made estimations of the masses $M_{12,\,3} \sin^3 i_3 = 1.05 \pm 0.02,\ 0.90 \pm 0.02\ M_\odot$ in a wide system and discussed possible determination of an astrometric orbit in the future data release of Gaia. Additionally, we propose an empirical method for measuring a period and minimal mass of contact systems, based on variation of the projected rotational velocity ($V \sin i$) from the spectra.

Key words: stars : fundamental parameters – binaries : eclipsing – binaries : spectroscopic – stars individual: T-Tau0-03027

1 INTRODUCTION

Contact binaries are a special type of eclipsing binaries, which have a distinct shape of the light curves (LC) and usually short periods. Thus they can be easily identified in photometrical surveys such as Transatlantic Exoplanet Survey (TrES) (Devor et al. 2008), Wide Angle Search for Planets (SuperWASP) (Pollacco et al. 2006), All Sky Automated Survey for SuperNovae (ASAS-SN) (Jayasinghe et al. 2018), Zwicky Transient Facility (ZTF) (Chen et al. 2020), Asteroid Terrestrial-impact Last Alert System (ATLAS) (Tonry et al. 2018; Heinze et al. 2018), Kepler (Borucki et al. 2010) and Transiting Exoplanet Survey Satellite (TESS) (Ricker et al. 2015). There is much evidence that the formation of such systems will require interaction with the third body (Pribulla & Rucinski 2006; D'Angelo et al. 2006; Rucinski et al. 2007), which can usually reveal itself

through third light (L3) (Liu et al. 2023) or LTTE (Hajdu et al. 2022). These systems are actually hierarchical triples, containing the inner system with a short period and another third star on the wide, long-period orbit (Czavalinga et al. 2023; Borkovits et al. 2025).

In this article we present the discovery and detailed study of such a triple system: J042901.09+254144.2, furthermore J04+25 (aka T-Tau0-03027; see other designations and basic info in Table 1), which was first discovered as an eclipsing binary in TrES data (Devor et al. 2008). It was observed during the binary-related time-domain sub-survey (TD-B) of LAMOST-MRS (Liu et al. 2020) and attracted our attention during the construction of the catalogue of spectroscopic orbits (Guo et al. 2025). We analyze available spectra and public photometry to confirm the presence of the third star and provide a consistent orbital solution for it. J04+25 is a rare case when an inner contact system is orbited by the brighter third

⋆ E-mail: mikhail.kovalev@ynao.ac.cn

Table 1. Designations and basic info from the literature: a-Gaia Collaboration et al. (2023a), b-Watson et al. (2006), c-Stassun et al. (2019), d-Jayasinghe et al. (2018), e-Devor et al. (2008), f-Kovalev et al. (2024b), g-Abdurro'uf et al. (2022).

Property	Value	Reference
Gaia DR3		a
source_id	151001777293928576	
$\alpha°$ ICRS	67.2545	
$\delta°$ ICRS	25.6955	
ϖ, mas	1.6581±0.1175	
$\mu_\alpha \cos \delta$, mas year^{-1}	1.363±0.143	
μ_δ, mas year^{-1}	-7.789±0.105	
G, mag	13.000±0.005	
RV, km s^{-1}	-44.25±4.43	
Variable Star indeX	163229	b
TESS input catalogue	TIC268143030	c
ASAS-SN	J042901.02+254144.6	d
TrES	T-Tau0-03027	e
LAMOST	J042901.09+254144.2	f
APOGEE	2M04290108+2541443	g

star with a relatively short period ($\sim$ 3 years), which allows us to measure precise masses.

The paper is organised as follows: in Section 2 we describe the observations. Section 3 describes the methods and presents our results. In Section 5 we discuss the results. In Section 6 we summarise the paper and draw conclusions. Throughout the paper we indicate components of the inner contact system by indices "1,2", while the third star has index "3". Inner orbit's parameters are referred to as "12", while outer orbit related parameters have index "3".

2 OBSERVATIONS

2.1 Spectra

LAMOST is a 4-meter quasi-meridian reflective Schmidt telescope with 4000 fibers installed on its 5° field of view focal plane. These configurations allow it to observe spectra for at most 4000 celestial objects simultaneously (Cui et al. 2012; Zhao et al. 2012). All available spectra were downloaded from www.lamost.org/dr11/ under the designation J042901.09+254144.2. We use the spectra taken at a resolving power of $R = \lambda/\Delta\lambda \sim 7\,500$. Each spectrum is divided into two arms: blue from 4950 Å to 5350 Å and red from 6300 Å to 6800 Å. We convert the heliocentric wavelength scale in the observed spectra from vacuum to air using PyAstronomy (Czesla et al. 2019) and apply zero point correction using values from Zhang et al. (2021). Observations are carried out from 2018-01-25 till 2023-02-04, covering 18 nights with a time base of 1836 days. The period is short ($P_{12} = 0.3642683$ d Devor et al. (2008)), thus we analysed spectra taken during short 20 minute exposures, ignoring co-added spectra. In total, we have 73 spectra, where the average signal-to-noise ratio (S/N) of a spectrum ranges from 8 to 32 pix^{-1} for the blue arm and from 16 to 70 pix^{-1} for the red arm of the spectrum, with the majority of the spectra having S/N around 40 pix^{-1}.

2.2 Photometry

We checked publicly available photometric archives for J04+25 and found datasets in TrES, SuperWASP, ASAS-SN, ZTF, WISE, ATLAS, Gaia, Kepler, and TESS. It was also observed during the Kilo-degree Extremely Little Telescope (KELT) survey (Oelkers et al. 2018), but LC data are not available.

Details on photometric datasets are provided in Table 2. Only Quick Look Pipeline (QLP (Huang et al. 2020a,b)) LCs were available for 70,71 sectors, so we used QLP results for 44,45 sectors for consistency.

3 METHODS & RESULTS

3.1 Spectral fitting

We analysed all spectra using the same single-star and binary model as in Kovalev et al. (2024b). Details on the synthetic spectral grid are provided in Appendix A. Here we provide a brief description and highlight updates which were necessary to fit spectra of the contact binary. The normalised binary model spectrum is generated as a sum of the two Doppler-shifted, normalised single-star model spectra $f_{\lambda,i}$ scaled according to the difference in luminosity, which is a function of the $T_{\rm eff}$ and visible stellar size. We use the following equation:

$$f_{\lambda,\rm binary} = \frac{f_{\lambda,2} + k_\lambda f_{\lambda,1}}{1 + k_\lambda}, \ k_\lambda = \frac{B_\lambda(T_{\rm eff,1})}{B_\lambda(T_{\rm eff,2})} k_R, \tag{1}$$

where k_λ is the luminosity ratio per wavelength unit, B_λ is the blackbody radiation (Planck function), $T_{\rm eff}$ is the effective temperature, k_R - light ratio coefficient. Throughout the paper, we always assume the first component to be the brighter one.

The binary model spectrum is later multiplied by the normalisation function, which is a linear combination of the first four Chebyshev polynomials (similar to Kovalev et al. 2019), defined separately for blue and red arms of the spectrum. The resulting spectrum is compared with the observed one using the scipy.optimise.curve_fit function, which provides optimal spectral parameters, radial velocities (RV) of each component plus the light ratio and two sets of four coefficients of Chebyshev polynomials. We keep metallicity equal for both components. In total, we have 18 free parameters for a binary fit.

In the top panel of Figure 1 we show the best fit examples by single-star and binary spectral models. We zoom into the wavelength range around the magnesium triplet, Hα and in a 70 Å interval in the red arm, where many iron lines are clearly visible. Although the single-star model fit generally looks good as it captures all narrow spectral lines, it has a problem around Mg triplet lines (5160-5190Å). The binary model fits it well because it has an additional fast rotating component, which takes into account the spectral contribution of both components in the contact system. Derived radial velocities (RV) for the primary allow us to get a single-line spectroscopic binary (SB1) orbit, see Section 3.1.1. We can see that the primary spectral component contributes around 65% in the spectrum, while the secondary component contributes to the remaining 35%, although due to the variability of the inner contact binary, these contributions change from one spectrum to another. The first spectral component has narrow spectral lines and shows almost no change in spectral parameters, while parameters for the second spectral component change very quickly, since it corresponds to the contact binary. This system has a "dumb-bell"

LC	N	filter	timebase, days	source	reference
SuperWASP	6679	*V*	1300	https://www.superwasp.org/	Butters et al. (2010)
TrES	1171	*V*	68	VizieR	Devor et al. (2008)
ATLAS	2376	*o*	3372	https://fallingstar-data.com/forcedphot/queue/	Shingles et al. (2021)
	842	*c*	3332		
ZTF	465	*g*	2161	https://irsa.ipac.caltech.edu/	Masci et al. (2019)
	681	*r*	2041		
ASAS-SN	665	*V*	2091	https://asas-sn.osu.edu/variables/206165	Jayasinghe et al. (2018)
	2091	*g*	2504		
WISE	208	*W1, W2*	4937	https://irsa.ipac.caltech.edu/	Cutri et al. (2013)
Gaia	32	*G*	919	https://www.cosmos.esa.int/gaia	Gaia Collaboration et al. (2023a)
Kepler K2	3430	K_P	80	MAST	Howell et al. (2014)
TESS 44	2845	*T*	24	MAST	Ricker et al. (2015)
TESS 45	2994	*T*	24		
TESS 70	9053	*T*	24		
TESS 71	9256	*T*	24		

Table 2. Public photometry. VizieR for TrES https://vizier.cds.unistra.fr/viz-bin/vizExec/Vgraph?J/AJ/135/850/T-Tau0-03027&P=0.36426830, MAST https://mast.stsci.edu/portal/Mashup/Clients/Mast/Portal.html
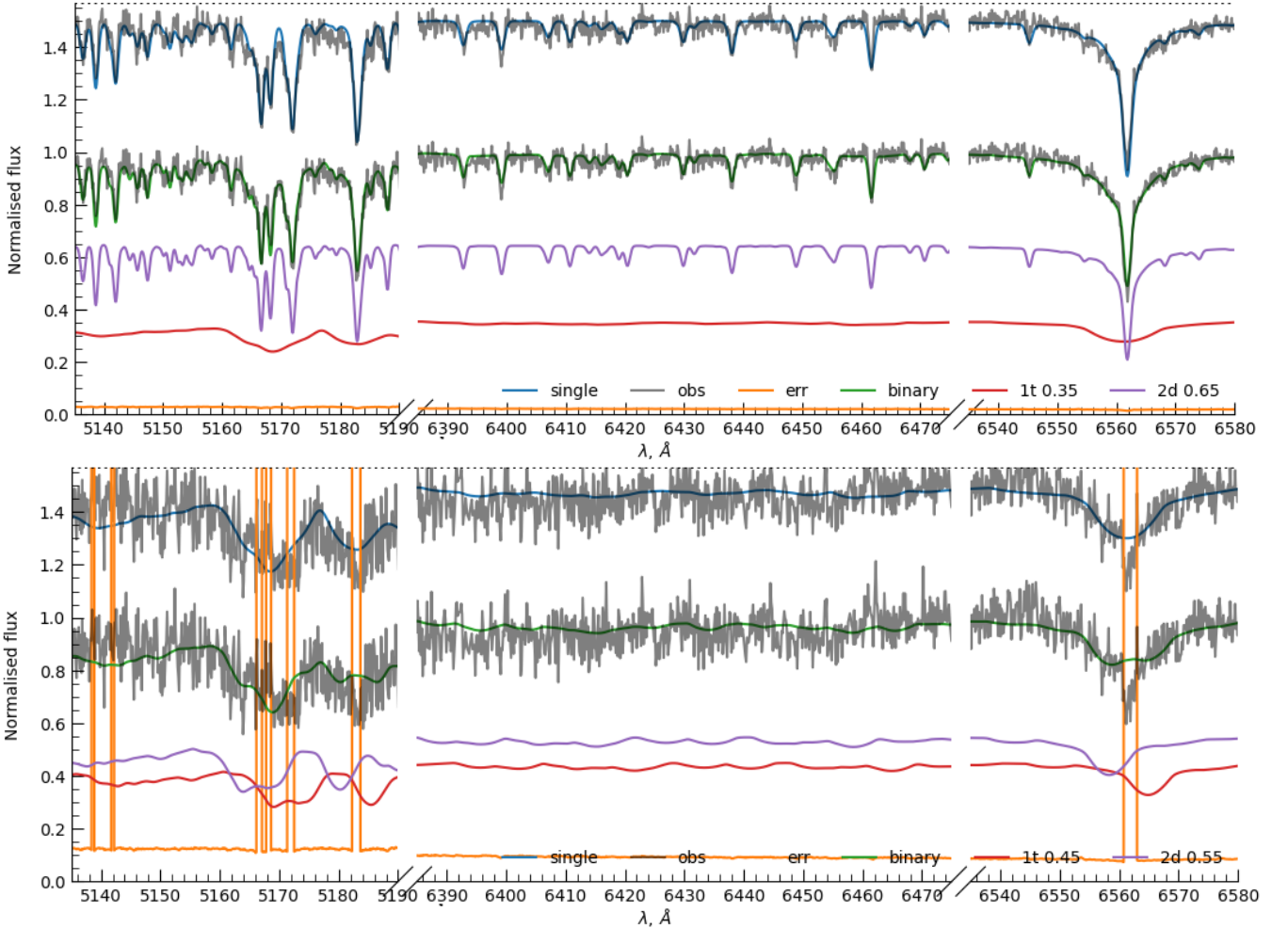
Figure 1. Example of the spectral fitting for spectrum taken at $\phi = 0.25$, MJD=59190.669 d. Original spectrum (top) and residual spectrum after subtraction of narrow-lined component (bottom). We zoom into the wavelength range around the magnesium triplet, Hα and in a 70 Å interval in the red arm. The observed spectrum is shown as a gray lines (with different offsets), the best fits are shown as a green (binary model with zero offset) and blue (single-star model with +0.5 offset) lines. The primary component is shown as the magenta line, the secondary as a red line. Their light contribution is also shown in legend. The errors are shown as an orange line.
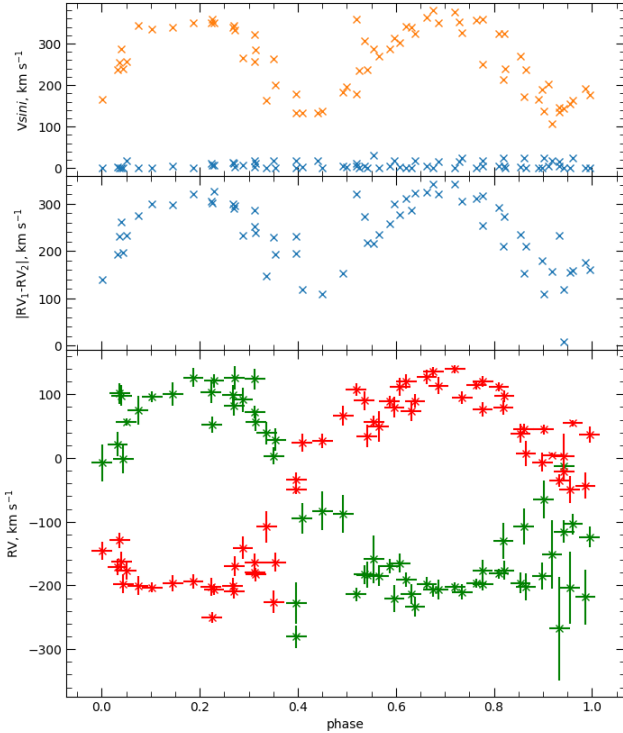
Figure 2. $V \sin i$ of the dim spectral component (orange crosses) and bright spectral component (blue crosses) are shown in top panel as a function of orbital phase, computed using ephemeris from ASAS-SN. Middle panel shows absolute difference of RV fitted from residual spectrum. Bottom panel shows RV, assigned to the both component of the contact system. Horizontal errorbars indicate half time of the exposure.

shape, so the fitted value of projected rotational velocity ($V \sin i$) will change according to the orbital phase computed using linear ephemeris from ASAS-SN (Jayasinghe et al. 2018):

$$t_{min}(\text{HJD}) = 2457391.91388 + 0.364277E, \qquad (2)$$

where E is an epoch (cycle number), see top panel in Figure 2. The bright spectral component has narrow spectral lines ($V \sin i < 20 \ \text{km s}^{-1}$), while the dim spectral component has $V \sin i \sim 150 \ \text{km s}^{-1}$ during eclipses and $V \sin i \sim 350 \ \text{km s}^{-1}$ at phases $\phi = 0.25, 0.75$, when we can see the contact system from the side.

In order to obtain the $RV_{1,2}$ of the individual components in the contact system, we need to separate the bright spectrum of the third star. This process is similar to opening the famous Russian doll "Matryoshka". At first, we use the original fit to get the bright, narrow-lined component of the binary model. Once we remove it, we can fit the remaining spectrum with the binary model again. We should increase the error spectrum for the residual spectrum according to its relative contribution in the original spectrum. For strongest spectral lines, subtraction was not perfect; therefore, we also increased errors for them to infinity. Once we fitted all residual spectra, we removed results for ten of them with S/N < 30 in the red arm, due to the bad performance of the binary model. We plot $|RV_1 - RV_2|$ as a function of orbital phase in the middle panel of the Figure 2. It is clear that $|RV_1 - RV_2|$ derived by the binary model correlates with $V \sin i$ values derived by the binary model for the contact system in the previous step. However, RVs need to be sorted because of confusion in the identification of primary/secondary

Table 3. Spectral parameters for all three stellar components.

Parameter	Star 1	Star 2	Star 3
T_{eff}, K	5637±342	5493±170	5847±38
log (g), cgs	4.13±0.41	3.96±0.46	3.73±0.13
[Fe/H], dex	-0.06 ± 0.13		-0.24±0.05
$V \sin i$, km s^{-1}	162±36	155±39	6±8

Table 4. GLS orbital solution for the third star.

parameter	value
P_3, day	944.4146±5.7816
t_{p3}, BMJD day	58588.0089±29.0809
e_3	0.038±0.017
ω_3, °	23±12
K_3, km s^{-1}	14.54±0.10
γ_3, km s^{-1}	-38.98±0.20

by the binary model. Thus RV were folded in a phase diagram and assigned to each component based on orbital phase, see the bottom panel in the Figure 2. As expected for the contact binary, they follow a circular orbit pattern, with roughly equal amplitudes. The motion of the center of mass causes additional scatter in RV, plus Rossiter-McLaughlin effect (Rossiter 1924; McLaughlin 1924) changes RV near eclipse phases. It is clear that individual values for radial velocities have low precision, especially for spectra taken near conjunction phases; however, large number statistics (63 measurements) will allow us to use these data in the further analysis, together with photometric data.

We computed weighted averages of T_{eff}, log (g), [Fe/H], $V \sin i$ for all three components using S/N in the red arm as a weight. These results are collected in Table 3. The third star is hotter than both components of the contact system and rotates much slower. Surface gravity log (g)$_3$ = 3.73±0.13 dex, however, it can be underestimated when derived only from LAMOST-MRS spectra, as it was shown in Kovalev et al. (2023). The third star has subsolar metallicity [Fe/H]$_3$ = -0.24 ± 0.05 dex. Metallicity of the contact system is larger then for the third star, although this is not very reliable result, since residual spectra are very noisy and no metal lines are visible due to significant rotational broadening.

3.1.1 GLS *orbit of the third star*

We can use radial velocities of the narrow-lined component, which corresponds to the third star, to calculate the orbital solution with Generalised Lomb-Scargle (GLS) code (Zechmeister & Kürster 2009). We choose 73 datapoints from the first output of the binary spectral model and feed them to GLS. Since the original GLS doesn't provide uncertainties for eccentricity (e_3) and periastron angle (ω_3) we refined the solution with the help of `scipy.optimise.curve_fit` function. The resulting orbit is given in Figure 3 and Table 4.

The third star has a slightly eccentric orbit ($e_3 = 0.04 \pm 0.02$) with a relatively long period $P_3 = 944 \pm 5$ days, which is significantly longer than the period of the inner contact system. Our orbit agrees with a single RV measurement from APOGEE DR17 (Abdurro'uf et al. 2022).
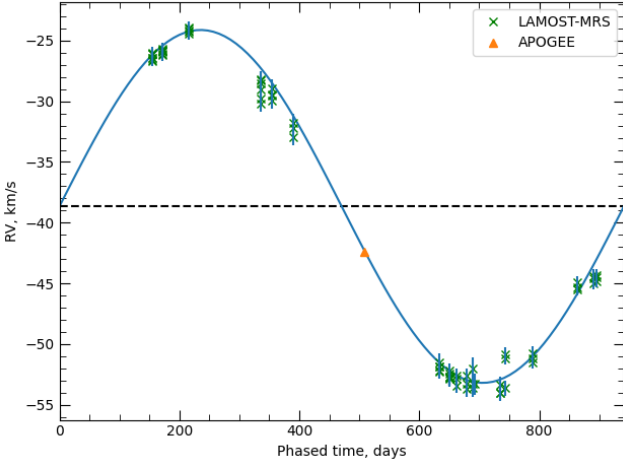
Figure 3. GLS orbital solution for the third star. Dashed horizontal line shows the systemic velocity. RV measurement from APOGEE DR17 Abdurro'uf et al. (2022) is shown as an orange triangle.

3.2 Modelling with W-D

We use the Wilson–Devinney program W-D (Wilson & Devinney 1971; Wilson 1979) with PYWD2015 (Güzel & Özdarcan 2020) user interface to make a "toy" model of LCs from TESS, KEPLER and ASAS-SN together with $RV_{1,2}$ from our spectral analysis. These datasets were fitted by the differential correction program in contact binary regime (MODE=3) with dimensionless potential Ω, inclination i_{12}, mass ratio q_{12}, semimajor axis $a = a_1 + a_2$, conjunction time $t_{0,12}$ as free parameters. For the third star orbit we assumed the simple case of a circular orbit with a fixed period $P_3 = 944$ days and $a_{12} + a_3, t_{0,3}$ as free parameters. The bandpass luminosity $L1$ of the primary component and third light $L3$ were also fitted, while the parameter $L2$ was fixed to 1 by the W-D. All other parameters were fixed, including the synchronicity parameters $F_{1,2} = 1$ and temperatures. We show the solution derived after 11 iterations in Figure 4 and Table 5. It is clear that our "toy" model is unable to properly fit all light variations, especially in K2 and TESS light curves. These LCs are affected by the O'Connell effect (O'Connell 1951), which is caused by spots on stellar surfaces. Residuals have different patterns for different LCs, so spot activity changes with time. ASAS-SN datasets have significantly lower precision and cover a longer time base; therefore, they are less affected by the O'Connell effect. Detailed analysis, including modelling of spots for K2 and TESS LCs will be done in the upcoming paper (Matekov et al in prep). Nevertheless, results of this analysis confirm the presence of the third star through significant contribution of L_3, which gradually decreases from $L3 = 78\%$ for ASAS-SN g down to $L3 = 68\%$ for TESS bands. This indicates that the third star is hotter than components of the contact system, which agrees with the findings from the spectra. Figure 4 shows that the third star's attraction causes significant motion to the barycentre of the contact system: RV solution oscillates around the systemic velocity and LC minima show periodic changes due to LTTE, which is clearly visible for ASAS-SN datasets. Therefore, we can perform O-C analysis for the times of minima.
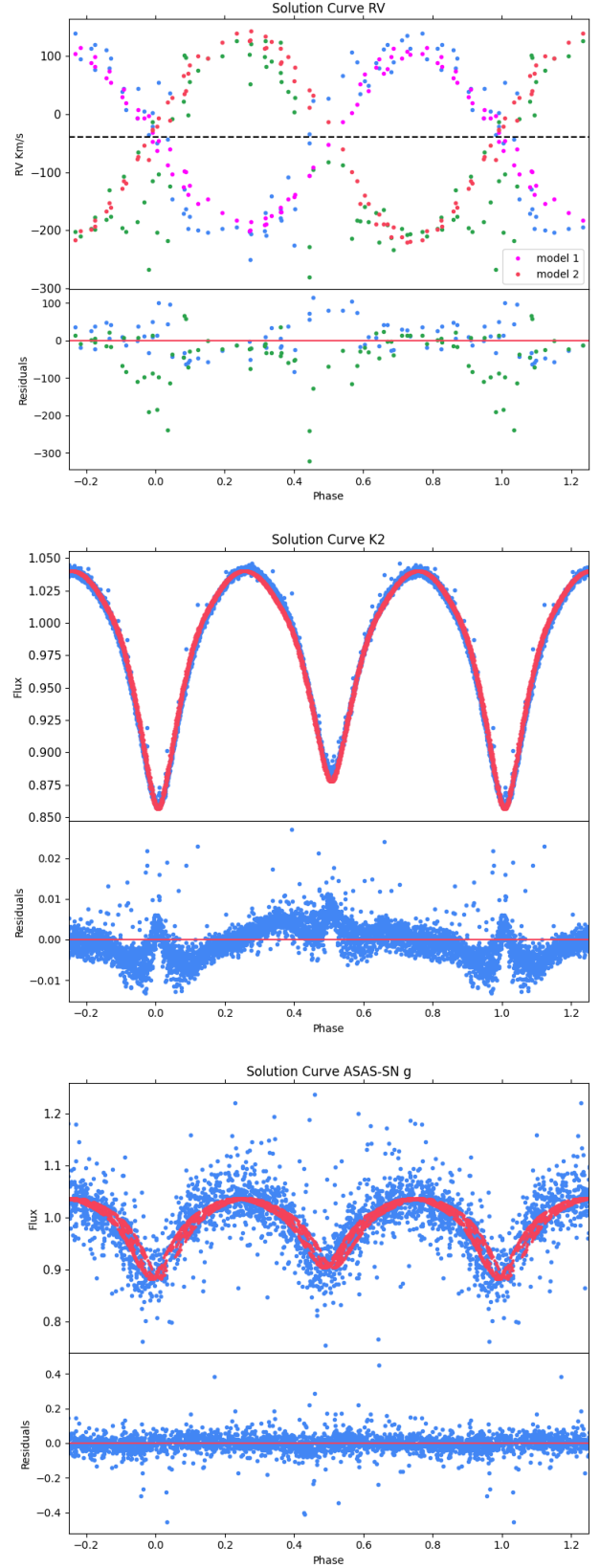

Figure 4. The "toy" model by W-D for K2, ASAS-SN g LCs and RV. Top panels show fit of the data, bottom panels show fit residuals.

Table 5. The "toy" model by W-D. Error estimates are standard errors from the differential correction program.

Parameter	W-D value
fixed:	
P_{12}, d	0.364277
e_{12}	0.0
$F_{1,2}$	1.0
$\alpha_{1,2}$	0.32
$A_{1,2}$	0.5
$T_{\text{eff}\,1,2}$, K	5700, 5500
γ_{12}, km s^{-1}	-38.98
P_3, d	944.0
e_3	0.0
i_3°	90
fitted:	
$a_1 + a_2$, $R_\odot$	2.468±0.055
i_{12}°	85.56±0.12
$\Omega_{1,2}$	3.458 ± 0.002
q_{12}	0.853±0.001
$t_{0,12}$, BMJD d	57391.75996± 0.00002
$a_{12} + a_3$, $R_\odot$	563.01±9.98
$t_{0,3}$, BMJD d	58033.13± 0.52
$L1_g$	1.80±0.03
$L1_V$	1.96±0.04
$L1_{K2}$	2.193±0.006
$L1_{T43}$	2.367±0.007
$L1_{T44}$	2.317±0.006
$L1_{T70}$	2.430±0.007
$L1_{T71}$	2.436±0.007
$L3_g$, per cent	78±1
$L3_V$, per cent	75±1
$L3_{K2}$, per cent	71.8±0.1
$L3_{T43}$, per cent	69.0±0.1
$L3_{T44}$, per cent	69.6±0.1
$L3_{T70}$, per cent	68.3±0.1
$L3_{T71}$, per cent	68.5±0.1
derived	
$M_{1,2}$, $M_\odot$	0.736, 0.615
$R_{1,2}$, $R_\odot$	0.962, 0.887
$\log{(g)}_{1,2}$, cgs	4.34, 4.33
$\log{L_{1,2}}$, $L_\odot$	-0.058, -0.190
r_1 (pole)	0.3760±0.0002
r_1 (side)	0.3970±0.0002
r_1 (back)	0.4305±0.0003
r_2 (pole)	0.3535±0.0004
r_2 (side)	0.3725±0.0005
r_2 (back)	0.4100±0.0009

3.3 O-C curve analysis

Unfortunately, our LC datasets mostly have sparse time coverage; therefore, one has to use data from long time intervals to get a good phase coverage of the light curve. Only for TESS data do we have enough time resolution to get times of the minima from every orbital cycle. Thus, we use template matching to get times of the minima, because it allows us to use LCs with sparse phase coverage and allows us to use a distinct shape of LC(Mikulášek et al. 2013). The linear ephemeris from Equation 2 was used to phase fold all datapoints from the selected time interval. The interval is selected only if it covers at least 90 per cent of the phases and contains more than 19 datapoints. We employ our "toy" model to generate a set of templates for Kepler, TESS, g and V bands. Then we use
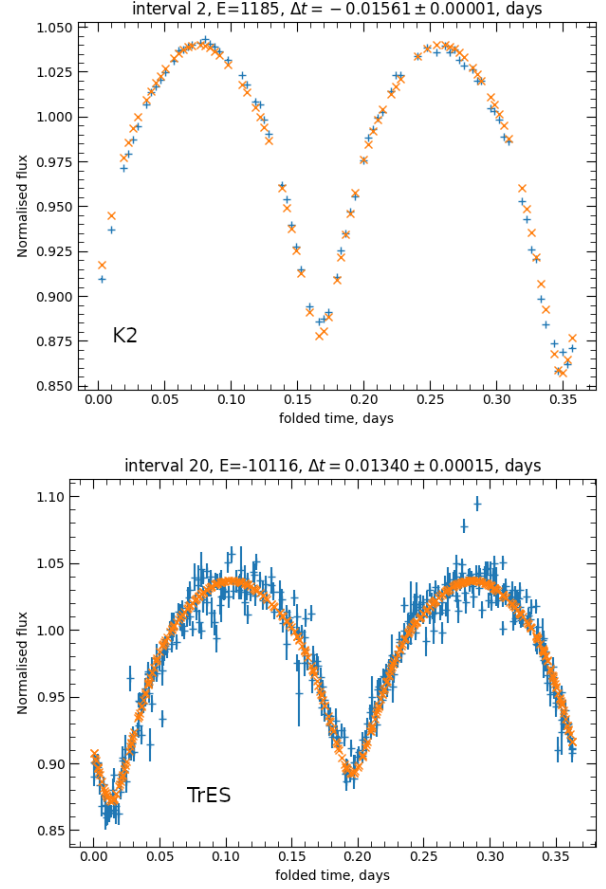
Figure 5. Plots illustrating our template matching algorithm for finding times of minima. Titles indicate duration of time interval, epoch, timeshift and its error. We show it for intervals in TrES, and K2 datasets.

SCIPY.OPTIMISE.CURVE_FIT function to find the optimal time shift of the relevant template, which is then linearly interpolated to match all datapoints from the interval. We select the integer number closest to the cycle number of the median time for a given interval as an epoch E. We show examples of template matching in Figure 5. The time shifts and their errors are the same as the primary minima and can be used for the O-C curve analysis.

The O-C curve is modelled using parabolic plus periodic variation, in a form of Keplerian orbit, which should take into account the LTTE effect.

$$O - C = \Delta t_0 + \Delta P\, E + \beta\, E^2 + W(p, E), \qquad (3)$$

where Δt_0, ΔP are corrections for linear ephemeris, β is a long-term change of the period and $W(p, E)$ is a periodic variation, where $p = A$, P_3, t_{p3}, e, ω are parameters of the Keplerian orbit. We used a built-in model from PyAstronomy(Czesla et al. 2019), which allows the computation of position and velocity along the line of sight for a two-body problem. Therefore, we fit both the O-C and RV$_3$ datasets simultaneously by adding systemic velocity γ and mass ratio $q_3 = \frac{M_1 + M_2}{M_3}$ to the fitted parameters. Also, we set $\omega_3^* = \omega_3 + 180°$ and $A = a_{12} \sin i_3 / c$ with $-c$ speed of light. We use only O-C from K2, TESS, TrES and SuperWASP, because they were computed using data from short time intervals ($\Delta T = 2$ days for K2, TESS and $\Delta T = 20$ days for TrES, SuperWASP), which are significantly smaller than the period ($P_3 \sim 944$ days) derived from

Table 6. Joint RV_3 and O-C curves fit. Estimates and errors are from median and standard deviations of EMCEE sampling.

Parameter	value
Δt_0, day	-0.0074±0.0001
ΔP, 10^{-6} day cycle^{-1}	-2.04±0.01
β, 10^{-11} day cycle^{-2}	-4.28±0.23
A, day	0.00632±0.00010
P_3, day	941.40±0.03
t_{p3}, (BMJD) day	58606.85±10.10
e_3	0.059±0.007
$\omega_3^{*\circ}$	210.3±3.1
$q_3 = \frac{M_1+M_2}{M_3}$	1.16 ± 0.01
γ_3, km s^{-1}	−39.00 ± 0.06

RV curve. We sample solutions with EMCEE (Foreman-Mackey et al. 2013) using 50 walkers and 25000 iterations. We present the resulting O-C curve fit in Figure 6, where we also show O-C values from ZTF, WISE, ASAS-SN, Gaia and ATLAS just for reference.

Table 6 lists parameters for joint fit models. We compute final values and their uncertainties as a median and standard deviation of EMCEE sampling, shown in Figure C1. This solution is consistent with GLS orbit, which was computed earlier, but precision is significantly improved. The contact system is heavier than the third star with mass ratio $q_3 = 1.16 \pm 0.01$. $\beta \neq 0$, thus the orbital period of the contact binary decreases at a rate of $dP/dt = -4.29 \cdot 10^{-8}$ d yr^{-1}. The updated linear ephemeris is:

$$t_{min}(\text{BJD}) = 2457391.90648 + 0.364275E, \qquad (4)$$

4 SED FITTING

The spectral energy distribution (SED) offers an independent approach to estimating system parameters like T_{eff} and distance d. We utilize the SEDFit package[1] for SED fitting, using BT-Settl (Allard et al. 2011) models to find the optimal fit. We use this software because it allows models with three components, plus it can use Gaia DR3 (Gaia Collaboration et al. 2023a) BP/RP spectrum. Unfortunately, current version doesn't provide uncertainties for fitted parameters. We impose constraints on the solution by fixing parameters of the contact system: $T_{eff\,1,2}$, $\log(g)_{1,2}$, $R_{1,2}$, $L3_{TESS} = 68\%$ from the LC solution (our "toy" model), while fitting for the distance d, extinction A_V, [Fe/H] and third star parameters ($T_{eff\,3}$, $\log(g)_3$, R_3).

In Figure 7, we present the resulting fit. Photometric measurements did not account for observations taken during eclipses, which may explain the small discrepancy. The estimated distance of $d = 619$ pc is larger than the single-star model value of $d = 487_{468}^{503}$ pc from Gaia DR3[2]. Other parameters are $A_V = 1.18$ mag, [Fe/H] = 0.05 dex, $T_{eff\,3} = 5800$ K, $\log(g)_3 = 4.31$ dex, $R_3 = 1.78$ $R_\odot$. They are quite different from our average spectroscopic values, but similar to Gaia DR3 single-star estimates $T_{eff} = 5620_{5595}^{5647}$ K, $\log(g) = 4.12_{4.10}^{4.14}$ dex, [M/H]= $-0.30_{-0.33}^{-0.28}$ dex, $R = 1.71_{1.65}^{1.77}$ $R_\odot$.

---

[1] https://github.com/mkounkel/SEDFit (Kounkel, M. 2023).
[2] GSP-Phot Aeneas best library using BP/RP spectra (distance_gspphot)

5 DISCUSSION

Results from joint RV_3 & O-C fitting allow us to get an estimate of the total mass ($M_{tot} = M_1 + M_2 + M_3$) using Kepler's third law:

$$M_{tot} \sin^3 i_3 = \frac{\left(c\,A\,\sqrt{1-e_3^2}\,(1+q_3)\right)^3}{GM_\odot}\left[\frac{2\pi}{P_3}\right]^2 = 1.95 \pm 0.03\ M_\odot, \qquad (5)$$

where $GM_\odot = 1.32712440041 \cdot 10^{20}$ m^3 s^{-2} - is the Solar mass parameter[3]. Thus, the contact system and the third star have masses $M_{12,\,3} \sin^3 i_3 = 1.05 \pm 0.02$, $0.90 \pm 0.02\ M_\odot$. Combining this with the mass of contact system $M_1 + M_2 = 1.351\ M_\odot$ from the "toy" model, we can get the approximation for $\sin i_3 = 0.9198$, so the inclination angle is $i_3 \sim 67°$.

Projected semimajor axes for the contact system and the third star are: $a_{12,\,3} \sin i_3 = 234 \pm 3$, $272 \pm 4\ R_\odot$. The angular separation between the contact system and the third star is around ~ 5 mas, if we use the Gaia DR3 distance $d = 486$ pc, which is too small to be resolved. However, photocenter should move relative to the center of mass with amplitude ~ 1 mas, slightly oscillating due to the variability of the contact system. Gaia DR3 Non-single star orbital catalog (Gaia Collaboration et al. 2023b) has many astrometric orbits with even smaller values of the semimajor axis, although now the astrometric orbit is absent for J04+25. Even if the orbit was computed, it was rejected as dubious by the filter on parallax significance, see Eq. 16 in Halbwachs et al. (2023). Possibly, variability of the contact system led to unreliable measurements of the photocenter position (renormalised unit weight error RUWE=6.029!), so Gaia was unable to determine a good astrometric orbit. Also, the current data release is based on observations with a time base covering only one full orbital period. We hope that the upcoming Gaia DR4 will provide an orbital solution for J04+25, so one can get an inclination of the wide orbit.

Third star is bright and close to the contact system, therefore theoretically we should be able to see its light reflected by the contact system. However only extremely precise space-based photometry will be sensible to this effect (reflected light ~ 3 ppm) which will be seen as a very small increase of $L3$ for illuminated phases.

5.1 Third star parameters from APOGEE

APOGEE DR17 (Abdurro'uf et al. 2022) has single-star estimates for this star: RV = -45.75 ± 0.05 km s^{-1}, $T_{eff} = 6343 \pm 46$ K, $\log(g) = 4.15 \pm 0.03$ dex, [M/H]=0.05 ± 0.01 dex, which corresponds to the third star. This result is based on high-resolution ($R = \lambda/\Delta\lambda = 22500$) infrared spectrum, although it should be biased as the single-star model fit did not take into account the dilution of the light by the contact system, see Figure 8. The contact system has nearly 'flat' spectrum due to fast rotation; therefore, the spectral contribution of the contact system can be easily removed during normalization of the original spectrum using a high-order polynomial function. We can see in Figure 8 that the contribution of the contact system was almost completely vanished by the normalisation. Thus we recommend the usage of the low-order polynomial for the normalisation of the spectrum, if we want to keep information about the contact system.

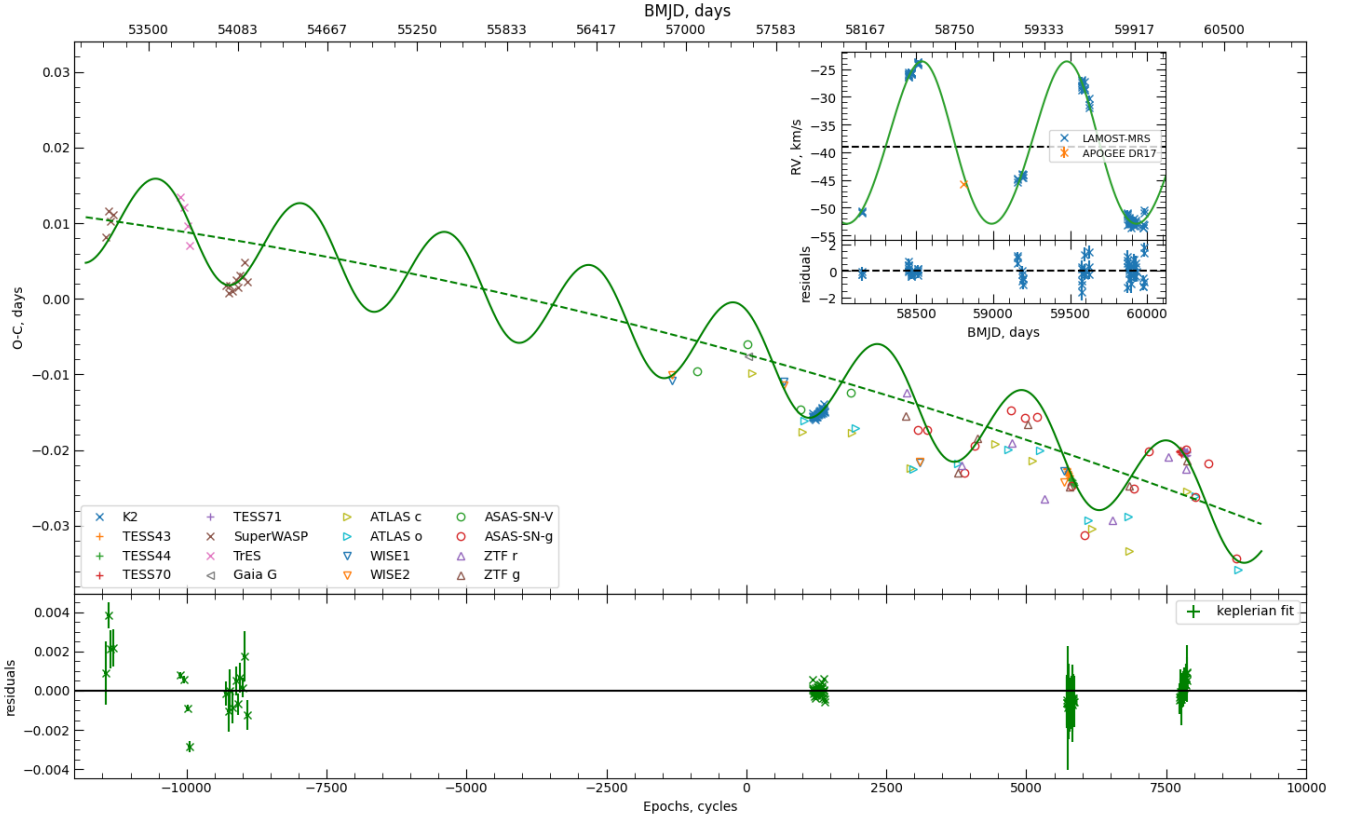[3] https://iau-a3.gitlab.io/NSFA/NSFA_cbe.html#GMS2012

Figure 6. Results for joint fit. O-C curve fit using parabola (dashed line) plus Keplerian orbit (solid line). Horizontal axes are shown with units in cycles (bottom) and BMJD (top) for convenience. Only K2, TESS, TrES and SuperWASP data are used in fitting, while others are shown for reference. RV_3 curve fit is shown on the inline plot. Dashed horizontal line shows the systemic velocity. RV measurement from APOGEE DR17 (Abdurro'uf et al. 2022) is also shown. Residuals for both fits are shown in the bottom panels.

5.2 GLS fit of $V \sin i$

$V \sin i$ values derived by the binary model in the first iteration correlate well with the absolute difference of radial velocities in the contact subsystem (see Figure 2). Linear fit is shown in the left panel of Figure 9:

$$|\Delta RV| = 13.52 \pm 10.25 + (0.81 \pm 0.04)V \sin i, \qquad (6)$$

It is similar to the empirical relation from Kovalev et al. (2022), but here we probe larger values of $V \sin i$: up to $\leq 400 \ \mathrm{km\,s^{-1}}$, while Kovalev et al. (2022) had $V \sin i < 300 \ \mathrm{km\,s^{-1}}$. We can try to use this correlation to get an approximation for the sum of radial velocity amplitudes $(K_1 + K_2) \sim |\Delta RV|_{max} \sim (V \sin i)_{max}$ and the period (Kovalev et al. 2024a). These two values can provide us minimal estimation of the subsystem mass $M_{contact} \sin^3 i$, using only spectroscopic data.

We run GLS, assuming circular orbit and find the best fit period $P_{V \sin i} = 0.182137 \pm 0.000001$ day, which is exactly half of the period from LC, see the right panel in Figure 9. Amplitude and offset are $K_{V \sin i} = 105 \pm 25 \ \mathrm{km\,s^{-1}}$ and $C_0 = 262 \pm 5 \ \mathrm{km\,s^{-1}}$ respectively. Using the linear relation we get $(K_1 + K_2) = 309 \pm 27 \ \mathrm{km\,s^{-1}}$, which together with doubled period provides us $M_{12} \sin^3 i_{12} = 1.12 \pm 0.30 \ M_\odot$. This value is consistent with $M_{12} \sin^3 i_3 = 1.05 \pm 0.02 \ M_\odot$ from the joint fit of the third star orbit.

6 CONCLUSIONS

J04+25 is an interesting case of hierarchical triple, where the third star is significantly brighter than the inner contact subsystem. Partial eclipses in the inner subsystem allow us to estimate third light and determine "light orbit" through LTTE, while the third star dominates in the spectra and can provide SB1 orbit. Joint fit of these data gives us complete information on the projection of the wide orbit on the line of sight. Extraction of RVs in the inner subsystem is a complex task for the traditional cross-correlation function (CCF) method because the third star dominates in the spectrum. Spectral disentangling (Ilijić 2017) can not be applied here, since light contributions of components change in every spectrum. Therefore, we determine RVs with iterative "Matryoshka"-like approach, using binary spectral model twice. This provides RVs consistent with our expectations for this contact binary.

Here we summarise our results:

(i) we successfully extracted radial velocities from medium resolution spectra for all three components, using binary spectral model in two steps. Third star RV have high precision and allow direct fitting of the orbit. Low precision of RV measurements in contact system is compensated by large number statistics. Thus we conclude that medium resolution spectra with low S/N still can be used to study contact binaries,

(ii) we built approximate "toy" model of the inner contact binary with third star using high quality photometry and RV. Although
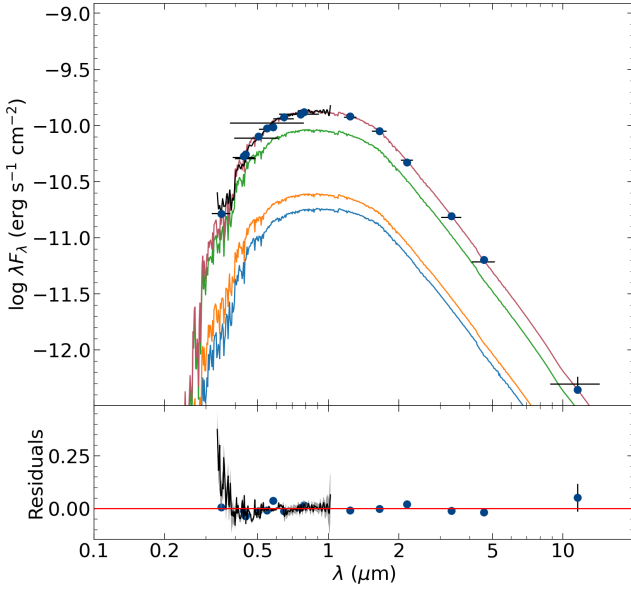
Figure 7. SED fitting with SEDFit. The top panel shows the observations, including Gaia DR3 BP/RP spectrum (black line), fluxes in Cousins, Gaia, 2MASS and WISE filters. Best fit SED of the whole system (red line), third star (green line), primary (orange line) and secondary (blue line) components of the contact system are also shown. The fit residuals are shown on the bottom panel.

this model can't properly fit all light variations in space-based LCs, it can serve as a good template for the searching of "light orbit" through LTTE. More detailed modelling, including spots, will be done in upcoming paper (Matekov et al in prep.),

(iii) we employed template matching technique to find periodic variation in several photometric datasets. This variation is consistent with third star orbit which was found earlier. Joint fit of RV and O-C curves allowed us to refine third star orbit.

(iv) we made estimations of the masses in wide system and discussed possible determination of astrometric orbit in the future data release of Gaia.

For this object we try to explore all potential of LAMOST-MRS data for the studying of the contact system. We find that even using spectra alone one can get estimations of the orbital period and the sum of radial velocity amplitudes, which taken together with Kepler's third law can provide minimal mass of the contact system. We plan to apply this method for the set of known contact binaries, observed by LAMOST-MRS.

DATA AVAILABILITY

The data underlying this article will be shared on reasonable request to the corresponding author.

REFERENCES

Abdurro'uf et al., 2022, ApJS, 259, 35
Allard F., Homeier D., Freytag B., 2011, in Johns-Krull C., Browning M. K., West A. A., eds, Astronomical Society of the Pacific Conference Series Vol. 448, 16th Cambridge Workshop on Cool Stars, Stellar Systems, and the Sun. p. 91 (arXiv:1011.5405), doi:10.48550/arXiv.1011.5405
Borkovits T., et al., 2025, A&A, 695, A209
Borucki W. J., et al., 2010, Science, 327, 977
Butters O. W., et al., 2010, A&A, 520, L10
Chen X., Wang S., Deng L., de Grijs R., Yang M., Tian H., 2020, ApJS, 249, 18
Cui X.-Q., et al., 2012, Research in Astronomy and Astrophysics, 12, 1197
Cutri R. M., et al., 2013, Explanatory Supplement to the AllWISE Data Release Products, Explanatory Supplement to the AllWISE Data Release Products, by R. M. Cutri et al.
Czavalinga D. R., Mitnyan T., Rappaport S. A., Borkovits T., Gagliano R., Omohundro M., Kristiansen M. H. K., Pál A., 2023, A&A, 670, A75
Czesla S., Schröter S., Schneider C. P., Huber K. F., Pfeifer F., Andreasen D. T., Zechmeister M., 2019, PyA: Python astronomy-related packages (ascl:1906.010)
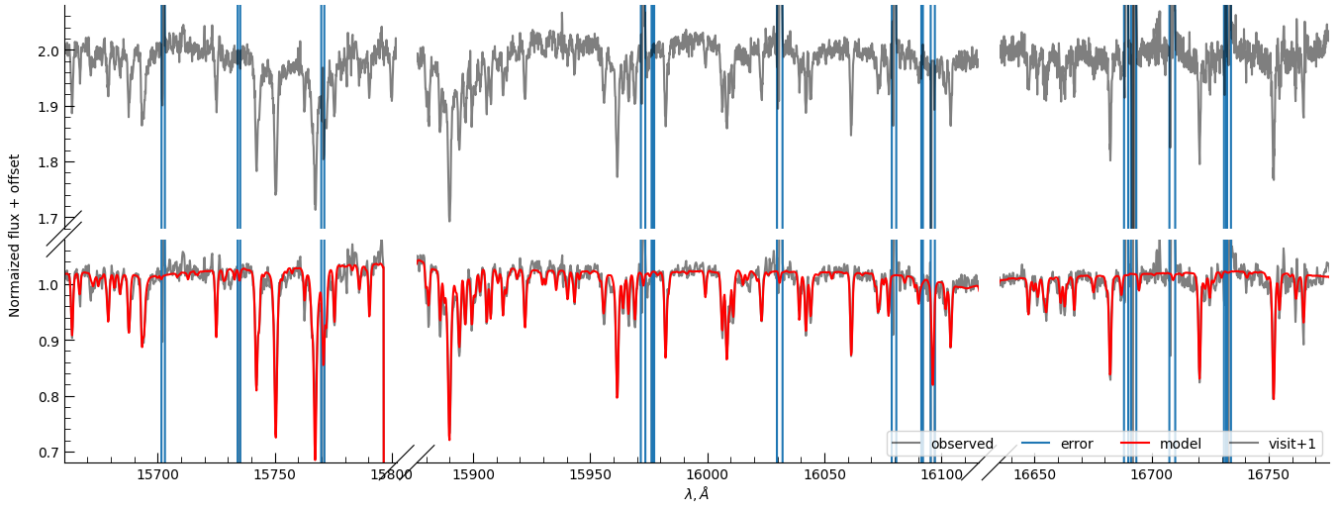
Figure 8. Parts of APOGEE DR17 ASPCAP spectrum (gray line) with best-fit model (red line) from SDSS Science Archive Server are shown on the lower panels. Visit spectrum normalized by the second order polynomial is shown on the top panels
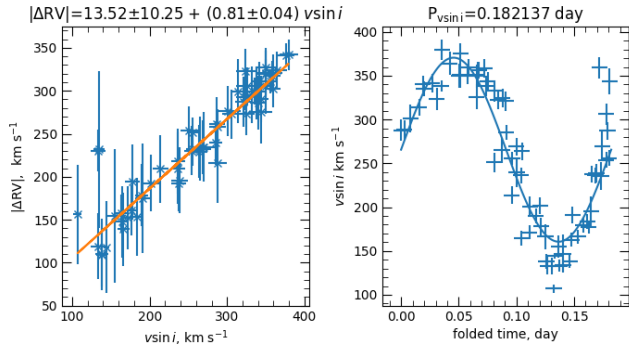

Figure 9. Correlation of $|\Delta RV|$ with $V \sin i$ (left panel). Best sine-fit of $V \sin i$ values of whole contact system by GLS (right panel).

D'Angelo C., van Kerkwijk M. H., Rucinski S. M., 2006, AJ, 132, 650

Devor J., Charbonneau D., O'Donovan F. T., Mandushev G., Torres G., 2008, AJ, 135, 850

Foreman-Mackey D., 2016, The Journal of Open Source Software, 1, 24

Foreman-Mackey D., Hogg D. W., Lang D., Goodman J., 2013, PASP, 125, 306

Gaia Collaboration et al., 2023a, A&A, 674, A1

Gaia Collaboration et al., 2023b, A&A, 674, A34

Grupp F., 2004a, A&A, 420, 289

Grupp F., 2004b, A&A, 426, 309

Guo S., et al., 2025, arXiv e-prints, p. arXiv:2504.11954

Güzel O., Özdarcan O., 2020, Contributions of the Astronomical Observatory Skalnate Pleso, 50, 535

Hajdu T., Matécsa B., Sallai J. M., Bódi A., 2022, MNRAS,

Halbwachs J.-L., et al., 2023, A&A, 674, A9

Heinze A. N., et al., 2018, AJ, 156, 241

Howell S. B., et al., 2014, PASP, 126, 398

Huang C. X., et al., 2020a, Research Notes of the American Astronomical Society, 4, 204

Huang C. X., et al., 2020b, Research Notes of the American Astronomical Society, 4, 206

Ilijić S., 2017, fd3: Spectral disentangling of double-lined spectroscopic binary stars, Astrophysics Source Code Library, record ascl:1705.012

(ascl:1705.012)

Jayasinghe T., et al., 2018, MNRAS, 477, 3145

Kounkel, M. 2023, mkounkel/SEDFit: 0.3, doi:10.5281/zenodo.8076501

Kovalev M., 2019, PhD thesis, Heidelberg University, doi:10.11588/heidok.00027411

Kovalev M., Bergemann M., Ting Y.-S., Rix H.-W., 2019, A&A, 628, A54

Kovalev M., Chen X., Han Z., 2022, MNRAS, 517, 356

Kovalev M., Wang S., Chen X., Han Z., 2023, MNRAS, 519, 5454

Kovalev M. Y., Chen X., Han Z., 2024a, Research Notes of the American Astronomical Society, 8, 175

Kovalev M., Zhou Z., Chen X., Han Z., 2024b, MNRAS, 527, 521

Liu C., et al., 2020, arXiv e-prints, p. arXiv:2005.07210

Liu N. P., Qian S. B., Liao W. P., Huang Y., Yuan Z. L., 2023, AJ, 165, 259

Masci F. J., et al., 2019, PASP, 131, 018003

McLaughlin D. B., 1924, ApJ, 60, 22

Mikulášek Z., Chrastina M., Zejda M., Janík J., Yhu L., Qian S., 2013, arXiv e-prints, p. arXiv:1311.0207

O'Connell D. J. K., 1951, Publications of the Riverview College Observatory, 2, 85

Oelkers R. J., et al., 2018, AJ, 155, 39

Pollacco D. L., et al., 2006, PASP, 118, 1407

Pribulla T., Rucinski S. M., 2006, AJ, 131, 2986

Ricker G. R., et al., 2015, Journal of Astronomical Telescopes, Instruments, and Systems, 1, 014003

Rossiter R. A., 1924, ApJ, 60, 15

Rucinski S. M., Pribulla T., van Kerkwijk M. H., 2007, AJ, 134, 2353

Shingles L., et al., 2021, Transient Name Server AstroNote, 7, 1

Stassun K. G., et al., 2019, AJ, 158, 138

Taylor M. B., 2005, in Shopbell P., Britton M., Ebert R., eds, Astronomical Society of the Pacific Conference Series Vol. 347, Astronomical Data Analysis Software and Systems XIV. p. 29

Tonry J. L., et al., 2018, PASP, 130, 064505

Watson C. L., Henden A. A., Price A., 2006, Society for Astronomical Sciences Annual Symposium, 25, 47

Wilson R. E., 1979, ApJ, 234, 1054

Wilson R. E., Devinney E. J., 1971, ApJ, 166, 605

Zechmeister M., Kürster M., 2009, A&A, 496, 577

Zhang B., et al., 2021, ApJS, 256, 14

Zhao G., Zhao Y.-H., Chu Y.-Q., Jing Y.-P., Deng L.-C., 2012, Research in Astronomy and Astrophysics, 12, 723

Table B1. Radial velocity measurements for third star. Full table is available online

time BMJD day	value km s^{-1}	error km s^{-1}
58143.4707	-50.8668	0.4356
58143.4874	-50.6238	0.3556
58143.5033	-50.8299	0.3556
..	..	..

Table B2. Radial velocity measurements for components in the contact subsystem. Full table is available online.

time BMJD day	RV$_1$ km s^{-1}	RV$_2$ km s^{-1}
58143.4874	49.9± 24.0	-184.7 ±16.5
58143.5033	111.9± 14.3	-164.8 ±15.0
58450.6503	119.7± 8.3	-197.8 ±9.5
..	..	..

Table B3. O-C values. Full table is available online.

LC	cycle	interval day	timeshift (O-C) day
K2	1180	2	-0.01510 ±0.00001
K2	1185	2	-0.01561 ±0.00001
K2	1191	2	-0.01549 ±0.00001
K2	1196	2	-0.01577 ±0.00001
..	..	..	..

APPENDIX A: SPECTRAL MODELS

The synthetic spectra are generated using NLTE MPIA online-interface https://nlte.mpia.de (see Chapter 4 in Kovalev 2019) on wavelength intervals 4870:5430 Å for the blue arm and 6200:6900 Å for the red arm with spectral resolution $R = 7500$. We use NLTE (non-local thermodynamic equilibrium) spectral synthesis for H, Mg I, Si I, Ca I, Ti I, Fe I and Fe II lines (see Chapter 4 in Kovalev 2019, for references).

The grid of models (6200 in total) is computed for points randomly selected in a range of $T_{\rm eff}$ between 4600 and 8800 K, log (g) between 1.0 and 4.8 (cgs units), $V \sin i$ from 1 to 300 km s^{-1} and [Fe/H][4] between −0.9 and +0.9 dex. The model is computed only if linear interpolation of the MAFAGS-OS(Grupp 2004a,b) stellar atmosphere is possible for a given point in parameter space. Microturbulence is fixed to $V_{\rm mic} = 2$ km s^{-1} for all models.

APPENDIX B: RV & O-C MEASUREMENTS

We provide the RV measurements in Tables B1, B2. O-C values are listed in Table B3.

[4] We used [Fe/H] as a proxy of overall metallicity, abundances for all elements are scaled with Fe.

APPENDIX C: EMCEE SAMPLE OF THE JOINT O-C&RV SOLUTION

In Figure C1 we show corner plot (Foreman-Mackey 2016) with EMCEE sampling results for the joint O-C&RV solution. We removed results in chains for four walkers, which got stuck in wrong periods.

This paper has been typeset from a TEX/LATEX file prepared by the author.
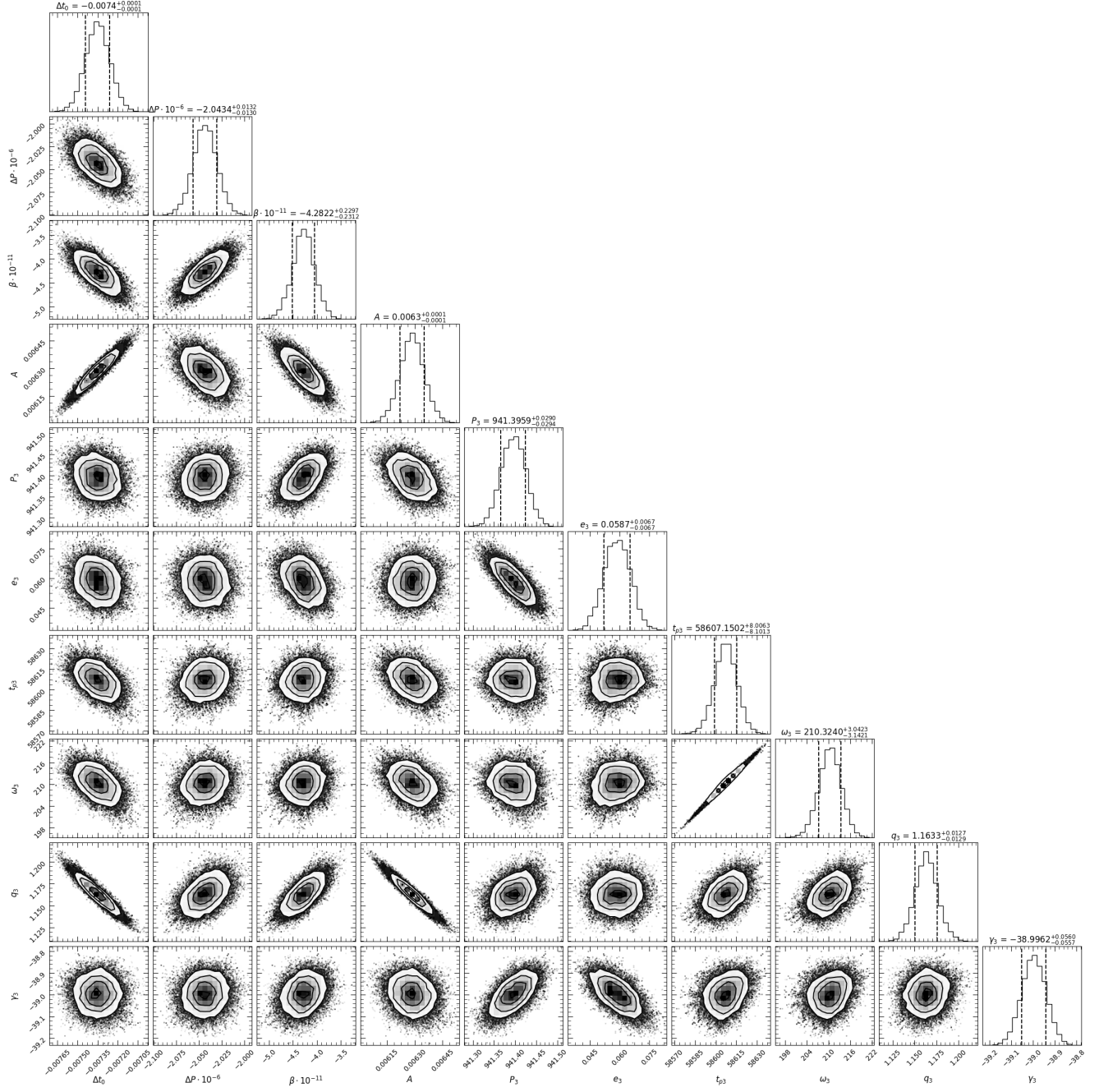
Figure C1. Corner plot for the sampling of the joint solution. Titles show 16, 50 and 84 percentiles.